S1 Supplementary material to section "Methods"

S1.1 Continental mean trends and volume budgets

This section describes the procedure used to derive continental water storage trends and volume balances from the G3P data.

The processing steps are as follows:

1. **Input data and significance filtering**
   Each grid cell is characterized by a linear trend estimate and its formal uncertainty (σ), derived from time series fitting, together with geographic coordinates. A grid cell is considered statistically significant when $|b|/\sigma$ exceeds the selected two-sided threshold: 2.58 for the primary 99% analysis and 1.96 for the 95% sensitivity analysis. Significance-filtered aggregates include only grid cells passing the respective threshold. For comparison, we additionally compute all-cell aggregates by integrating all grid cells for which trends have been estimated.

2. **Geolocation and area calculation**
   The native 0.5° G3P field is sampled at every second grid point, and the resulting 1° grid is used as the integration grid. Grid centres are assigned to continents using the Natural Earth Admin-0 Countries 1:110m shapefile (`ne_110m_admin_0_countries.shp`). If a grid centre falls outside a country polygon, it is assigned to the nearest valid land-country polygon using planar longitude–latitude distance in degrees; this fallback is used only for continent classification. Grid-cell areas are calculated independently and geodetically on the WGS84 ellipsoid. Country-to-continent assignments follow the Natural Earth `CONTINENT` attribute, except for Russia. Russian grid cells west of 60°E are assigned to Europe and those at or east of 60°E to Asia. Russian coastal and Arctic cells represented in the shapefile are treated cellwise by longitude. Greenland and Antarctica are excluded from both TWS and GWS aggregation. The GWS aggregation additionally excludes a defined Canadian Arctic Archipelago polygon with vertices (longitude, latitude) $(-93.47, 72.04)$, $(-75.19, 62.80)$, $(-60.60, 61.13)$, $(-59.00, 83.76)$, $(-108.24, 83.16)$, and $(-107.00, 76.45)$, closed back to the first vertex. The same cells are retained in TWS. This mask removes approximately 1.0×10^6 km^2 of nominal grid-cell area from the GWS aggregation relative to TWS.

3. **Physical volume integration**
   For the tabulated trend column, continental trends are reported as area-weighted means over significant grid cells. Continental volume change rates are computed independently by spatial integration of significant grid-cell trends:

$$\Delta V = \sum_i A_i \cdot b_i \cdot 10^{-6}. \tag{S1}$$

   where b_i denotes the grid-cell trend (mm yr^{-1} equivalent water height) and A_i the corresponding grid-cell area (km^2). The factor 10^{-6} converts mm km^2 to km^3, yielding volume change rates in km^3 yr^{-1} (numerically equivalent to Gt yr^{-1} for freshwater). Positive and negative contributions are integrated separately to obtain gains, losses, and the net balance (ΔV). Because volume changes are obtained by direct summation of grid-cell contributions, they are physically additive.

4. **Global aggregation and validation**
   Global mean trends (mm yr^{-1}) are computed as significant-area-weighted averages of continental trend estimates, while global volume changes are obtained by summing continental volume contributions. Mass-balance consistency is verified by ensuring that Gain – Loss $\approx \Delta V$.

S2 Supplementary material to section "Results"

S2.1 Supplementary material to section "Time-domain clustering"

Figure S1 shows the exploratory K-means clustering of TWS time-series. As in the GWS clustering, the grouping is based only on structural similarity of the time series and does not include trend estimates, trend uncertainties, or significance information. The clusters therefore describe dominant temporal regimes rather than hydrological process classes.

The background seasonal/interannual variability cluster covers large parts of the continents and shows no pronounced coherent long-term decline in the cluster-mean time series. A second cluster, seasonal variability with weak drying, shows stronger seasonal variability together with a weak negative tendency and occurs in several regions of Europe, North America, and Asia. Two tropical seasonal clusters are separated mainly by the phase and amplitude of the annual cycle. The northern-tropical / monsoonal seasonality cluster includes regions where the annual storage maximum follows monsoonal or northern-tropical wet-season timing, whereas the southern-tropical high-amplitude seasonality cluster includes regions such as the Amazon Basin and Zambezi region, where seasonal TWS amplitudes are particularly large and phase-shifted relative to the northern-tropical regime. The mixed depletion / cryosphere-influenced decline cluster groups regions with pronounced negative TWS behaviour arising from different sources, including surface-water decline, groundwater depletion, and cryospheric mass loss. The strongest cryosphere-dominated TWS decline is isolated in the strong cryospheric mass loss cluster, which includes glacier and ice-rich regions such as the Gulf of Alaska and parts of the Canadian Arctic. The formal trend significance and volumetric storage-change budgets are derived from the grid-cell trend analysis.

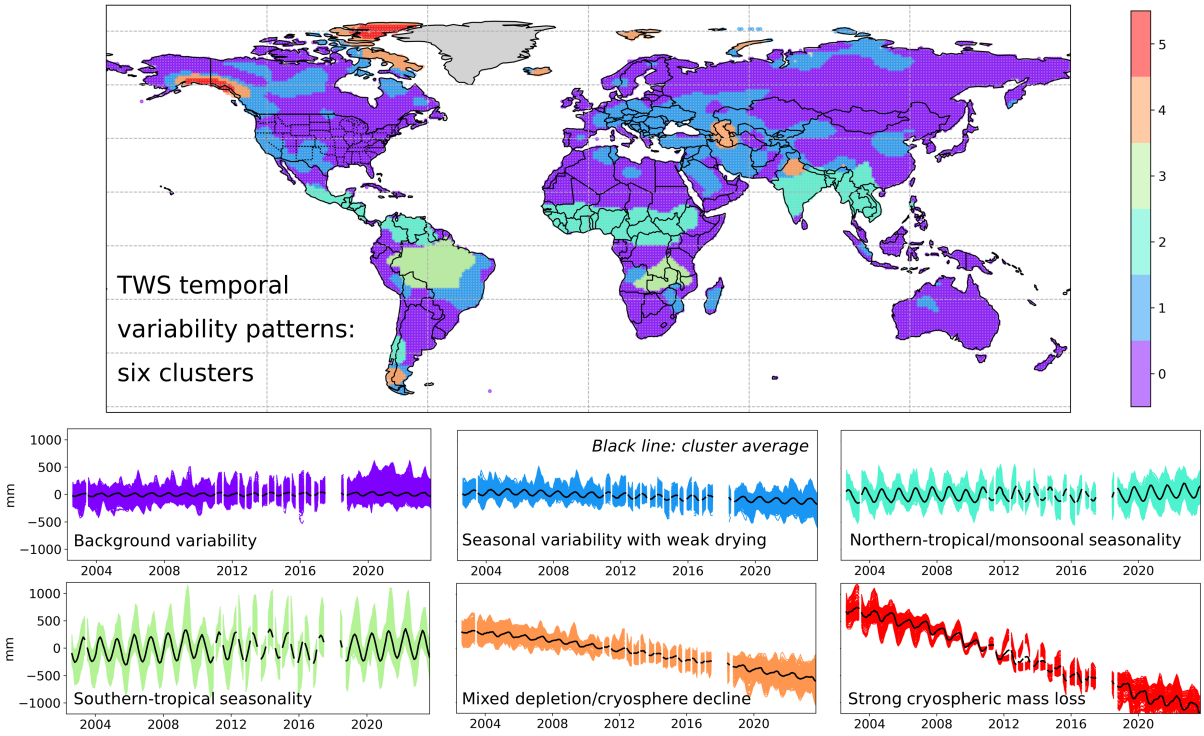


Figure S1: Exploratory K-means clustering of terrestrial water storage (TWS) time-series from the G3P data. The map shows the spatial distribution of six clusters, and the sub-panels show the corresponding cluster time series with descriptive cluster names. The black line represents the cluster-mean time series. The two tropical seasonal clusters differ mainly in the phase and amplitude of the annual cycle, reflecting different timing of regional wet seasons and storage maxima. Units are millimetres of equivalent water height.

S2.2 Supplementary material to section "Spectral analysis"

The spectral analysis in the main paper compares the globally averaged PSDs of TWS, GWS, and the modelled non-groundwater storage components before and after removal of the fitted deterministic signals. It shows that GWS is the dominant storage-component signal across most of the analysed frequency range. Glacier mass exceeds the GWS contribution only at the very lowest frequencies, where strong long-term glacier-storage trends dominate. The supplementary analysis presented here provides a more detailed discussion, plus a detailed comparison of GWS and RZSM, and distinguishes the effects of removing periodic terms from the additional effect of removing the linear trend.

In the main-text comparison, differences between the PSDs of the original time series and the post-fit residuals reflect the spectral power associated with the fitted trends and periodic signals, together with leakage around these deterministic components. The strongest reduction at the lowest frequencies occurs for glacier mass, consistent with the pronounced glacier trends discussed in the main text. Clear trend-related reductions are also visible for TWS, SWS, and GWS, whereas the additional effect of detrending is comparatively weak for RZSM and SWE. The relative importance of the non-groundwater storage components varies with frequency. Among these components, RZSM exhibits the largest spectral amplitudes across much of the interannual band below 1 cpy, except at the very lowest frequencies below approximately 0.1 cpy, where glacier mass dominates. SWE and SWS show broadly similar magnitudes at long to intermediate periods up to approximately 0.3 cpy and lie near the lower end of the component spectra. Towards 1 cpy, SWE approaches the RZSM spectral level. At frequencies above 1 cpy, RZSM and SWE form the dominant non-groundwater contributions, whereas SWS remains generally weaker but approaches comparable amplitudes near 6 cpy. The glacier-mass spectrum decreases more strongly towards higher frequencies.

Despite these frequency-dependent contributions from the modelled non-groundwater components, GWS retains the largest spectral amplitudes among the individual storage components across most of the analysed frequency range. It therefore represents the dominant storage-component contribution to TWS variability over most of the spectrum, while glacier mass dominates the trend-related signal at the lowest frequencies. Here, dominance refers to the relative spectral amplitudes of the individual component time series and not to an exact additive decomposition of the TWS PSD, because cross-spectral covariance between components may also contribute to the TWS spectrum.

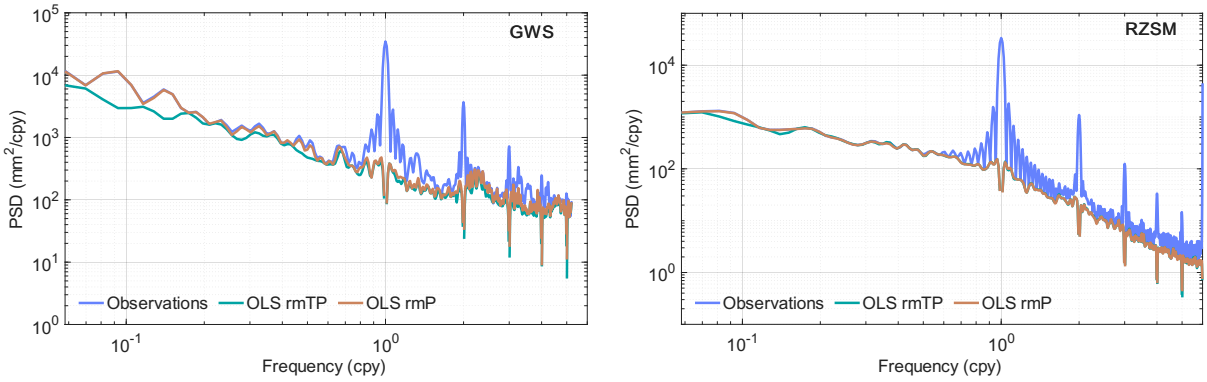


Figure S2: Globally averaged power spectral densities (PSDs) of groundwater storage (GWS; left) and root-zone soil moisture (RZSM; right), shown for the original time series, after removal of the fitted periodic terms (rmP), and after removal of both the fitted linear trend and periodic terms (rmTP).

Figure S2 illustrates the separate effects of periodic signal and trend removal for GWS and RZSM. For RZSM, removal of the periodic terms produces the dominant change in spectral

shape. The annual and semi-annual peaks and their surrounding side lobes are strongly reduced, whereas subsequent removal of the linear trend causes only a small additional decrease in low-frequency power. This indicates that globally averaged RZSM variability is governed primarily by seasonal and interannual variations, with a comparatively weak contribution from the fitted linear trend.

GWS exhibits a different response. Removal of the periodic terms reduces the annual and semi-annual peaks and associated leakage, while subsequent trend removal produces a further pronounced reduction at the lowest frequencies. The GWS spectrum therefore contains a substantially stronger trend-related low-frequency component than the RZSM spectrum. At the same time, low-frequency power remains after removal of the deterministic terms, indicating persistent stochastic GWS variability. Broadened peaks and residual side lobes remain around the annual and semi-annual frequencies in both GWS and RZSM. These structures can result from time-variable seasonal amplitudes and phases. Amplitude modulation of the annual cycle produces cyclostationary sidebands, including spectral power in the 2–3 and 3–4 cpy bands (Hamlington et al., 2019; Chandanpurkar et al., 2021). ENSO-related interannual variability may additionally modulate the amplitude or phase of seasonal water-storage variations and affect the resulting sidebands (Cheon et al., 2021).

Generally speaking, seasonal hydrological variability is also not necessarily represented by a small number of stationary sinusoidal terms. Monsoon-dominated regions such as India can exhibit strongly asymmetric recharge–discharge cycles, while parts of central Africa show secondary seasonal maxima. Such non-sinusoidal and multi-seasonal behaviour produces higher-harmonic and inter-harmonic spectral power that cannot be removed completely by annual and semi-annual terms. Temporal gaps can further broaden spectral peaks and side lobes (Thomson, 1982). These non-stationary and non-harmonic characteristics of TWS variability have also been identified as relevant targets for future satellite-gravity missions (Jensen et al., 2020).

At frequencies above approximately 3–4 cpy, the flattening of the spectra, as shown in the main text body, indicates an increasing white-noise-type contribution. The remaining high-frequency structure is expected to have a very limited influence on linear trend uncertainties only, as these are controlled primarily by low-frequency spectral power. GWS is the dominant storage-component signal across most of the TWS spectrum and contains pronounced trend-related and persistent low-frequency variability. RZSM is more strongly controlled by seasonal and interannual variability and constitutes the dominant non-groundwater component over much of that frequency range. Together with the component-wise comparison in the main text, these findings support the use of a power-law-plus-white-noise model for GWS and an AR(1)-plus-white-noise model for RZSM.

S2.3 Residual distribution analysis

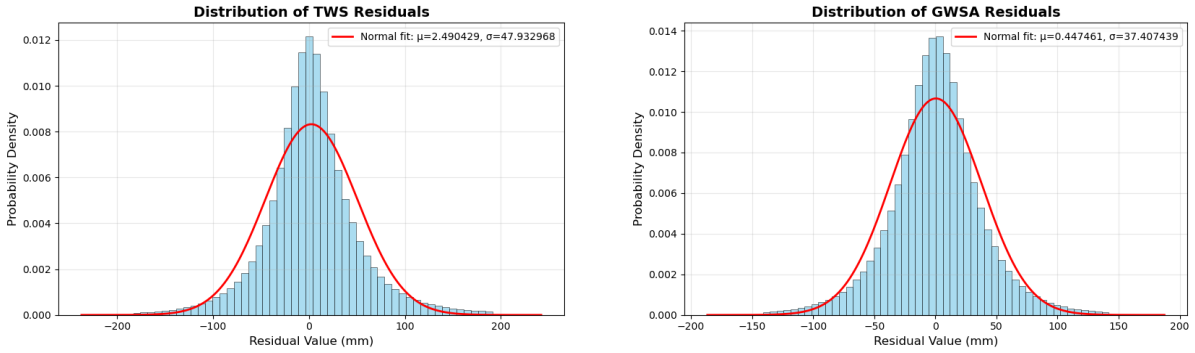


Figure S3: GRACE water storage residuals from all grid cells, shown as empirical and fitted distributions. To avoid distortion of the histogram scaling by a small number of extreme values, residuals beyond $\pm 3\sigma$ are omitted from the visualization. Normal distributions are fitted to the residuals. The empirical distributions are somewhat more peaked and slightly heavier-tailed than the fitted normal distributions. Since the significance test relies on the approximate normality of the estimated trend rather than of the individual residuals (under the central limit theorem), this has a limited effect on the trend-significance assessment.

S2.4 Stochastic model parameters and distributions

This section presents auxiliary stochastic-model parameters and trend estimates for the TWS and GWS grid-cell time series. Large negative values of κ (top panels) reflect strong correlations, and result in larger trend uncertainty (middle panels). For completeness, the bottom panels show the estimated trends (without significance indication). Figure S6 shows the distributions of Figs. S4 and S5. The medians in the top panel indicate that the estimated κ values for both TWS and GWS lie between flicker and random-walk noise, with a correlation reduction from the TWS-to-GWS computation step (resulting from the removal of interannual signals). This also leads to a median GWS trend uncertainty (1 sigma) of about 2.6 $\mathrm{mm\,yr^{-1}}$ (Fig. S6, middle panel). The bottom panel shows that GWS trends are smaller, which mostly results from the removal of ice mass trends by the TWS-to-GWS reduction step.

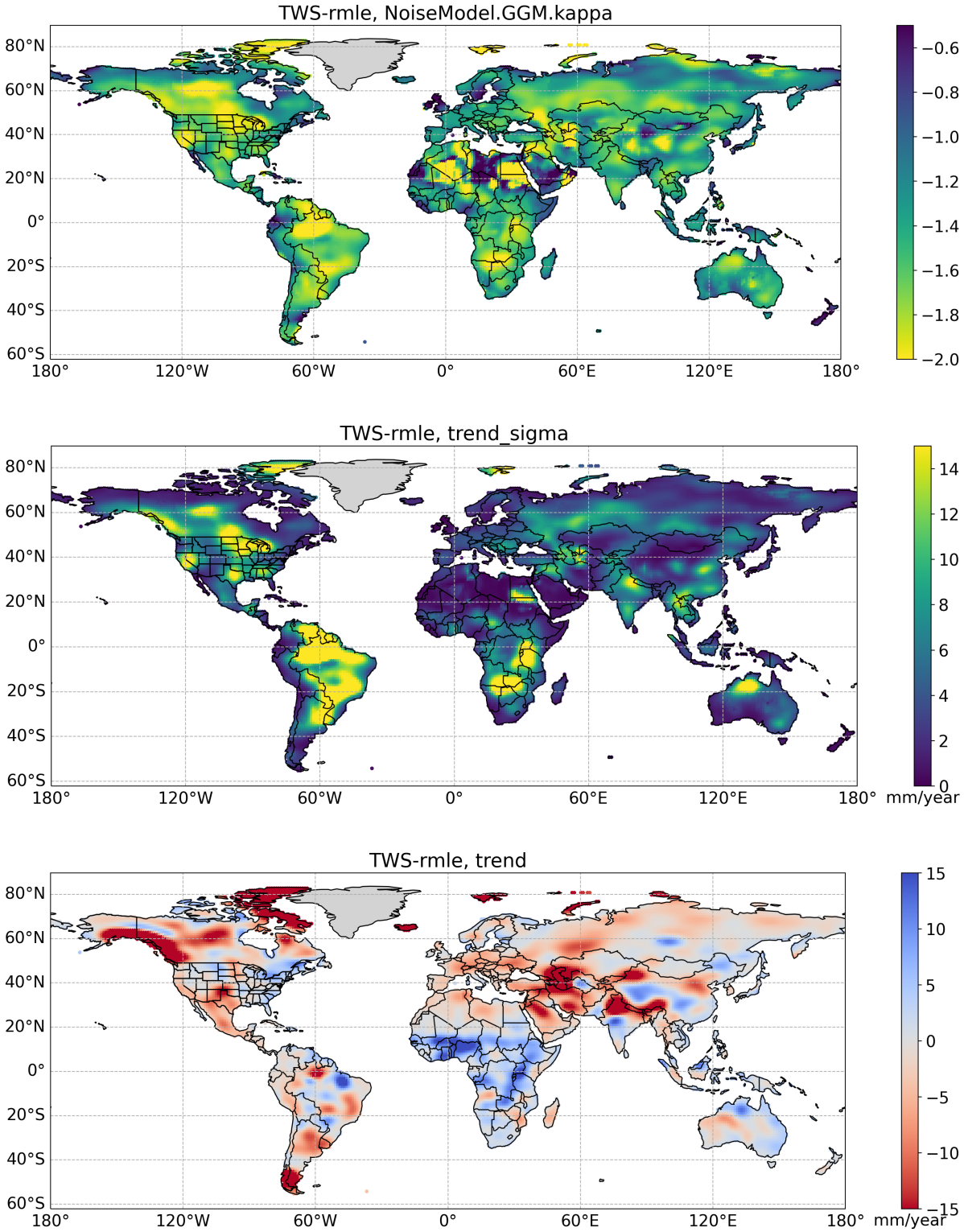


Figure S4: Estimated power law κ coefficient (top panel), trend uncertainties (1-sigma, middle panel) and trends (bottom panel) for TWS.

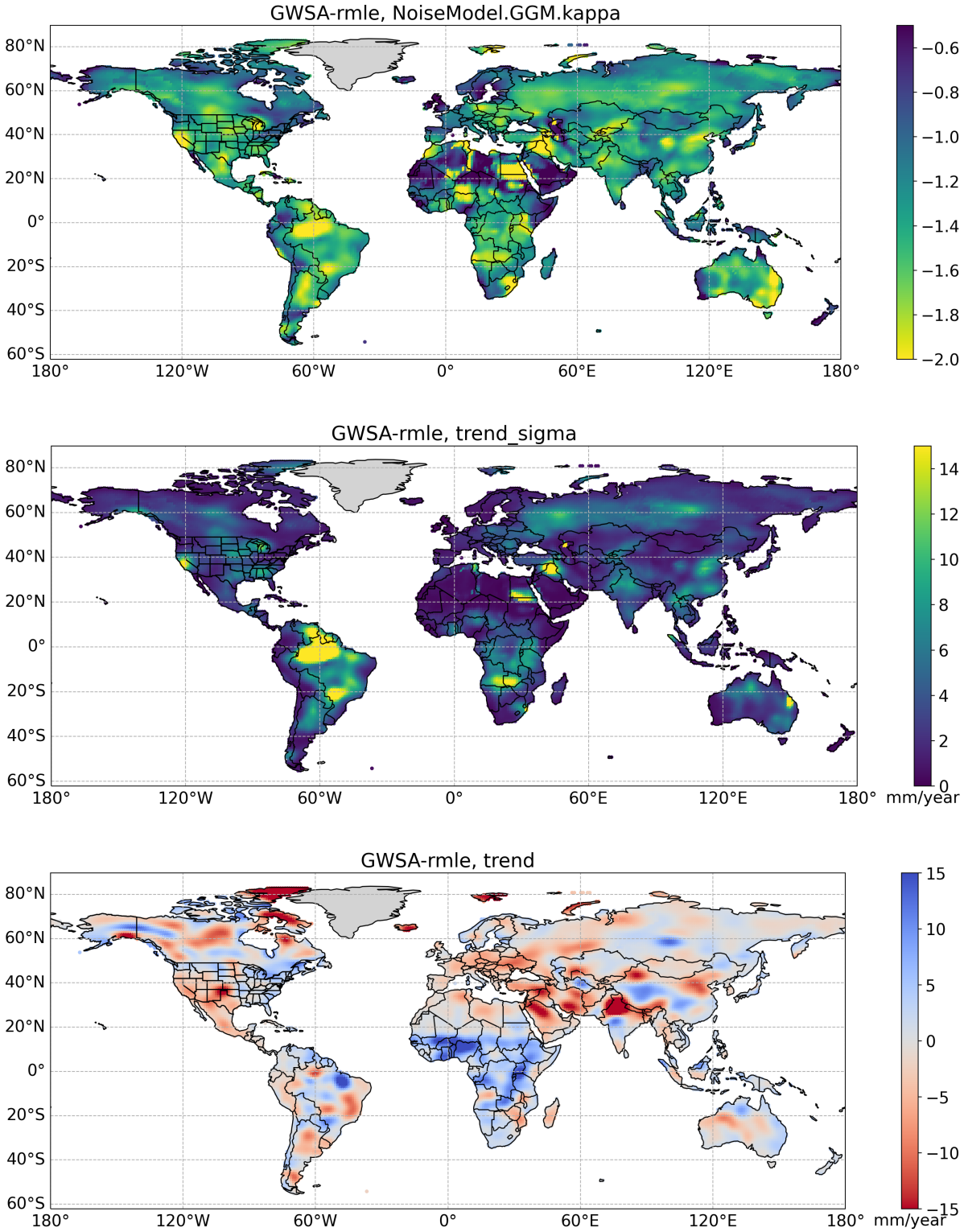


Figure S5: Estimated power law κ coefficient (top panel), trend uncertainties (1-sigma, middle panel) and trends (bottom panel) for GWS.

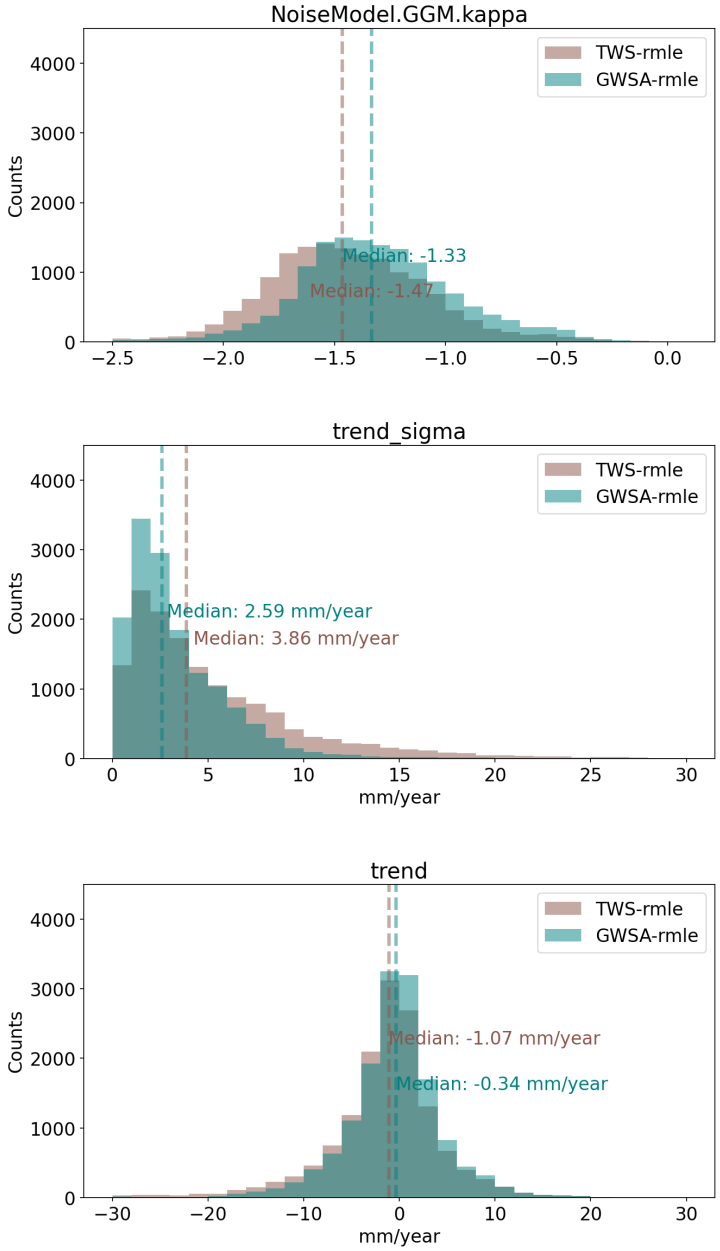


Figure S6: Histogram comparison of estimated power law κ coefficients (top panel), trend uncertainties (1-sigma, middle panel), and trends (bottom panel) for TWS and GWS, from Figs. S4 and S5.

S2.5 95% significance trends

To assess the sensitivity of the detected GWS trends to the chosen significance threshold, Fig. S7 shows the global distribution of significant TWS and GWS trends using a 95% confidence level (1.96 threshold). Overall, lowering the confidence threshold does not substantially alter the large-scale spatial patterns identified in the main analysis. As expected, areas of significant trends expand modestly, for example around Mexico City.

In Europe, the 95% threshold highlights more spatially continuous regions of significant drying, particularly in southern Germany and the Alpine region (Switzerland and Austria). More generally, a slightly larger fraction of grid cells approaches or exceeds significance in the Northern Hemisphere than in the Southern Hemisphere. This indicates that Northern Hemisphere groundwater signals are often closer to the detection threshold, consistent with

stronger long-term trends and/or lower relative noise levels, but does not change the overall interpretation of the results. Tables S1 and S2 report on the continentally aggregated trends and changes for the 95% confidence level.

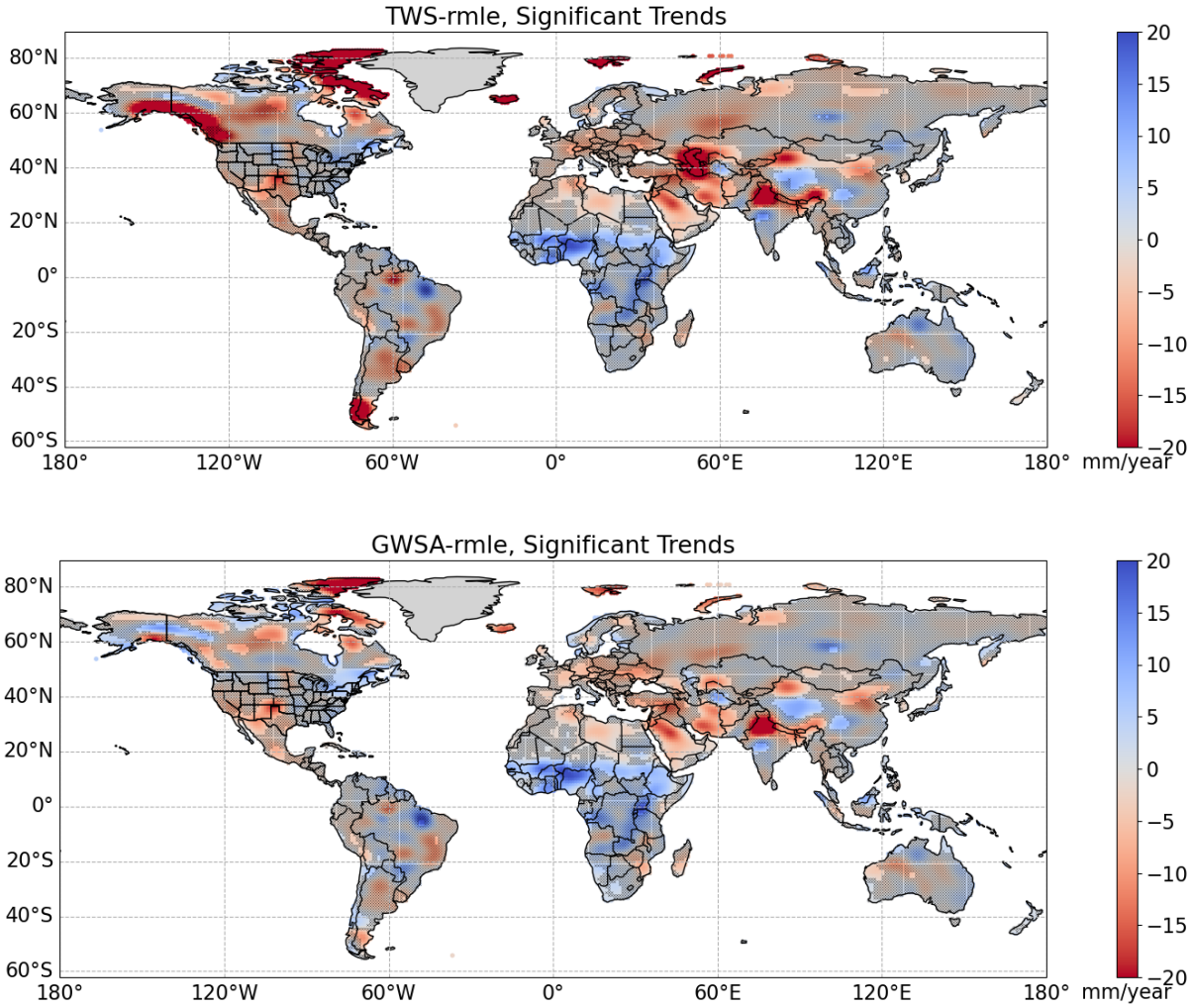


Figure S7: Significant TWS (top panel) and GWS trends (bottom panel) using a 95% confidence level. Shading with "X" represents data with insignificant trends, while all non-shaded trends represent statistically significant trends.

Table S1: TWS trend statistics by continent. Significant trends: $|\text{trend}|/\sigma \geq 1.96$ (95% confidence level). The mean trend is the area-weighted mean over significant grid cells. Grid cells inside the defined Canadian Arctic Archipelago mask are retained in the TWS aggregation.

Region	Areal Coverage			Mean Trend	Volume Change		
	Area (10^6 km^2)	**Sig. Area** (10^6 km^2)	**Sig. Frac.**	**Trend** (mm yr^{-1})	**Gain** (km^3 yr^{-1})	**Loss** (km^3 yr^{-1})	ΔV (km^3 yr^{-1})
Africa	29.9	8.3	0.3	4.1	43.2	9.2	34.0
Asia	44.4	11.5	0.3	-8.8	13.2	114.2	-100.9
Europe	10.0	1.3	0.1	-13.2	1.1	17.6	-16.5
North America	22.2	5.1	0.2	-19.3	6.0	105.3	-99.3
Oceania	8.4	0.6	0.1	0.6	0.9	0.6	0.3
South America	17.6	1.1	0.1	-16.0	0.3	17.6	-17.3
Global	**132.5**	**27.9**	**0.2**	**-7.2**	**64.8**	**264.5**	**-199.7**

Table S2: GWS trend statistics by continent. Significant trends: $|\text{trend}|/\sigma \geq 1.96$ (95% confidence level). The mean trend is the area-weighted mean over significant grid cells. The defined Canadian Arctic Archipelago mask is excluded from the GWS aggregation.

Region	Areal Coverage			Mean Trend	Volume Change		
	Area (10^6 km^2)	**Sig. Area** (10^6 km^2)	**Sig. Frac.**	**Trend** (mm yr^{-1})	**Gain** (km^3 yr^{-1})	**Loss** (km^3 yr^{-1})	ΔV (km^3 yr^{-1})
Africa	29.9	11.3	0.4	4.1	56.9	10.7	46.2
Asia	44.4	11.5	0.3	-5.3	17.8	78.7	-60.8
Europe	10.0	2.2	0.2	-3.8	1.8	10.3	-8.5
North America	21.2	6.3	0.3	-1.4	16.3	24.9	-8.6
Oceania	8.4	1.0	0.1	0.2	1.5	1.2	0.2
South America	17.6	1.2	0.1	0.0	3.0	3.1	0.0
Global	**131.5**	**33.6**	**0.3**	**-0.9**	**97.4**	**128.8**	**-31.4**

Table S3: TWS all-cell trend statistics by continent. All retained grid cells with trend estimates are included without significance filtering. The mean trend is the area-weighted mean over all retained grid cells. Grid cells inside the defined Canadian Arctic Archipelago mask are retained in the TWS aggregation.

Region	**Area** (10^6 km^2)	**Trend** (mm yr^{-1})	**Gain** (km^3 yr^{-1})	**Loss** (km^3 yr^{-1})	ΔV (km^3 yr^{-1})
Africa	29.9	2.7	101.6	20.4	81.2
Asia	44.4	-3.2	40.8	181.3	-140.5
Europe	10.0	-4.2	3.1	44.8	-41.6
North America	22.2	-6.2	19.4	157.1	-137.8
Oceania	8.4	0.8	14.2	7.5	6.7
South America	17.6	-2.1	21.4	58.3	-36.9
Global	**132.5**	**-2.0**	**200.5**	**469.4**	**-268.9**

Table S4: GWS all-cell trend statistics by continent. All retained grid cells with trend estimates are included without significance filtering. The mean trend is the area-weighted mean over all retained grid cells. The defined Canadian Arctic Archipelago mask is excluded from the GWS aggregation.

Region	**Area** (10^6 km^2)	**Trend** (mm yr^{-1})	**Gain** (km^3 yr^{-1})	**Loss** (km^3 yr^{-1})	ΔV (km^3 yr^{-1})
Africa	29.9	2.9	105.0	18.8	86.2
Asia	44.4	-1.8	45.4	123.7	-78.3
Europe	10.0	-2.7	3.6	30.4	-26.8
North America	21.2	-1.0	29.3	49.5	-20.2
Oceania	8.4	-0.0	9.7	9.9	-0.2
South America	17.6	-0.0	30.3	30.4	-0.1
Global	**131.5**	**-0.3**	**223.2**	**262.6**	**-39.3**

S2.6 Model evaluation and trend sensitivity

S2.6.1 Evaluation of the stochastic models

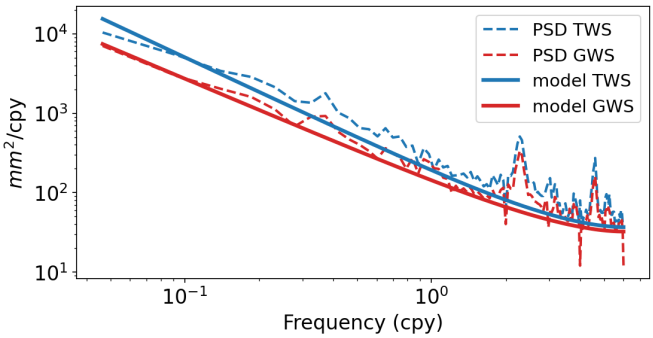


Figure S8: Globally averaged power spectral densities (PSDs) of the TWS and GWS residuals (dashed lines), together with the corresponding power-law-plus-white-noise model spectra (solid lines).

To evaluate the post-fit adequacy of the stochastic models used for trend detection and water-storage-change quantification, we compare the globally averaged empirical residual PSDs with the corresponding power-law-plus-white-noise model spectra (Fig. S8). The residual spectra exhibit clear power-law behaviour, while spectral amplitudes are reduced across the frequency range after separation of the modelled non-groundwater storage components.

The power-law-white-noise models reproduce the empirical PSDs well at low and intermediate frequencies, particularly below approximately 1 cpy. This includes the low-frequency range that primarily controls long-term trend uncertainty. Remaining intra-seasonal variability is less well represented at higher frequencies, but is expected to have only a limited influence on the estimated trend uncertainties, which are governed mainly by low-frequency spectral power (e.g., Bos et al., 2020).

S2.6.2 Sensitivity of groundwater storage trends to regression method

A comparison of OLS and GLS trend estimates illustrates the sensitivity of the derived GWS trends to the treatment of temporal covariance (Fig. S9). The OLS estimates yield a near-zero global area-weighted mean of -0.08 mm yr^{-1} and a slightly positive grid-cell median of 0.22 mm yr^{-1}. The GLS estimates produce a more consistently negative distribution, with an area-weighted mean of -0.36 mm yr^{-1} and a grid-cell median of -0.16 mm yr^{-1}.

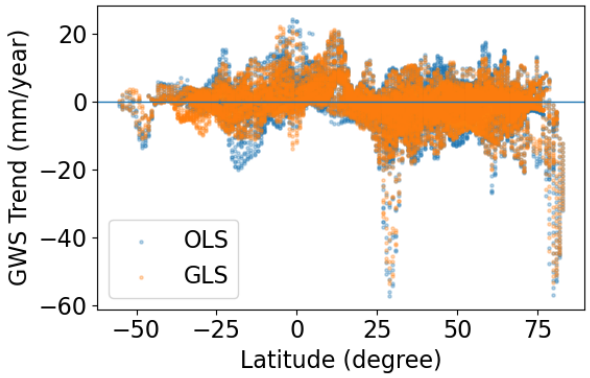


Figure S9: Latitudinal distribution of groundwater-storage trends estimated using ordinary least squares (OLS) and generalized least squares (GLS). Each point represents the trend of one grid cell plotted against latitude; horizontal lines indicate zero trend.

The GLS-derived trends also exhibit a narrower distribution than the OLS estimates. This difference reflects the incorporation of the estimated temporal covariance into the deterministic model fit, which changes the relative influence of observations affected by persistent residual variability; this is especially visible for latitudes between -30 and 0 degrees, resulting from a strong influence of inter-annual variations in South America. The global mean and median are shifted toward more negative values by approximately 0.3–0.4 mm yr^{-1} under GLS relative to OLS, although the differences remain small in absolute magnitude at the global scale.

References

Bos, M.S., Montillet, J.P., Williams, S.D., Fernandes, R.M., 2020. Introduction to geodetic time series analysis, in: Geodetic Time Series Analysis in Earth Sciences. Springer, pp. 29–52.

Chandanpurkar, H.A., Fasullo, J.T., Reager, J.T., Hamlington, B.D., 2021. A note on spectral representation of cyclostationary GRACE-TWS signals. Geophysical Research Letters 48, e2021GL093278. doi:10.1029/2021GL093278.

Cheon, S.H., Hamlington, B.D., Reager, J.T., Chandanpurkar, H.A., 2021. Identifying ENSO-related interannual and decadal variability on terrestrial water storage. Scientific Reports 11, 13595. doi:10.1038/s41598-021-92729-4.

Hamlington, B.D., Reager, J.T., Chandanpurkar, H.A., Kim, K.Y., 2019. Amplitude modulation of seasonal variability in terrestrial water storage. Geophysical Research Letters 46, 4404–4412. doi:10.1029/2019GL082272.

Jensen, L., Eicker, A., Dobslaw, H., Pail, R., 2020. Emerging changes in terrestrial water storage variability as a target for future satellite gravity missions. Remote Sensing 12, 3898. doi:10.3390/rs12233898.

Thomson, D.J., 1982. Spectrum estimation and harmonic analysis. Proceedings of the IEEE 70, 1055–1096. doi:10.1109/PROC.1982.12433.